Modeling of Piezoelectric Tube Actuators

Osamah M. El Rifai, and Kamal Youcef-Toumi
Department of Mechanical Engineering
Massachusetts Institute of Technology
77 Massachusetts Avenue Room 3-348,
Cambridge, MA 02139, USA.
Tel:617-258-6785, Fax:617-258-6575
osamah@mit.edu, youcef@mit.edu

***Abstract*— A new dynamic model is presented for piezoelectric tube actuators commonly used in high-precision instruments. The model captures coupling between motions in all three axes such as bending motion due to a supposedly pure extension of the actuator. Both hysteresis and creep phenomena are included in the overall actuator model permitting modeling nonlinear sensitivity in the voltage to displacement response. Experimental data on hysteresis and creep are presented to support the modeling. Experiments and model predictions show that due to coupling a voltage V_z corresponding to vertical displacement will produce lateral displacement that acts as a disturbance to the main lateral response. The resonance frequency for the lateral dynamics is inherently lower than that of the longitudinal dynamics. Therefore, V_z is expected to contain frequencies that may excite the lateral resonance. Accordingly, this out of bandwidth disturbance will not be well compensated for either in open or closed loop control of the actuator. In order to preserve performance in open loop actuator control and stability and performance in closed loop control, a large reduction in the bandwidth of vertical motion would be required to avoid exciting the first bending mode.**

I. Introduction

Piezoelectric actuators can provide sub-nanometer displacement and achieve a high-bandwidth. As a result, they are used in many high-precision motion applications such as micro and nano-positioning motion stages. Therefore, there has been extensive work in the literature on dynamic models of piezoelectric actuators. Piezoelectric actuators come in many different forms and shapes inc;uding tube actuators. The tube actuator offer a compact design, three degrees of freedom motion, and low-cost of construction. These desirable features have made tube actuators widely used in precision instruments such as scanning probe microscopes (SPM).

Several physically-based models for the tube actuator are available in the litreture such as [1]–[3]. Other researchers [4], [5], have presented models that were based on experimentally identified data for motion in a single axis. These models however, describe the dynamics of an ideal uncoupled tube, ignoring coupling between motion of different axes. This coupling would be of great impact on system performance especially if the actuator was to be part of a feedback system. In addition, these models describe the fast mechanical dynamics of the piezoelectric actuator ignoring creep effects which are of paramount importance to positioning repeatability in open loop operation such as in most SPM. Furthermore, hysteresis and nonlinear voltage to displacement sensitivity are not captured by the aforementioned models. Therefore, there is a strong need for an accurate dynamic model that accurately captures these key characteristics of the tube actuator. This is the objective of this paper.

The paper is organized as follows. Section II presents modeling results. In Section II-A, a model for the actuator's lateral dynamics will be presented, while actuator longitudinal dynamics are presented in Section II-B. Section II-C, discusses and presents how a hysteresis model would be correctly incorporated in the overall model of the tube. Supporting experimental data is also presented. A creep model is presented in Section II-D along with experimental results. Discussion is given in Section III, while summary and concluding remarks are given in Section IV.

II. Piezoelectric Tube Model

The piezoelectric actuator shown in Figure 1, is a thin-walled tube. The tube has four electrodes of equal segments on its outer surface, and either a single or four electrodes on its inner surface. Applying a voltage to its inner electrode(s) results in longitudinal motion along the Z axis. Motion in the X or Y direction is typically generated by subjecting two opposite electrodes to two voltage signals that have the same magnitude but 180^o out of phase. The tube is generally used with one end fixed and the other end is free to position a load. Therefore, a mass m_o representing lumped mass of a load and a reaction force $F_r(t)$ are included in the model at the tube's free end.

A. Piezoelectric Tube Lateral Dynamics

Models avialable in the literature are for an ideal uncoupled tube actuator. Due to inevitable machining tolerances, some eccentricity is always present in the tube, typically a maximum of $50\,\mu m$ for a $12.7\,mm$ diameter tube [6]. This seemingly small eccentricity could be in fact significant when the actuator is used in precision instruments with nanometer resolution. The newly developed model presented within is based on two eccentric cylinders, as shown in Figure 2, with eccentricity δ_x and δ_y from the geometric center of the outer cylinder O_o.

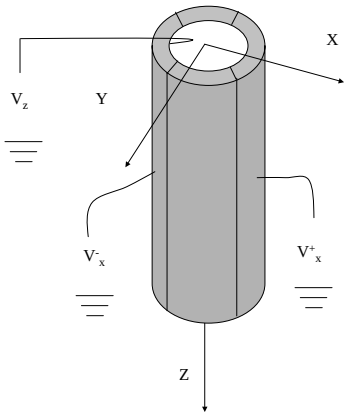

Fig. 1. Piezoelectric tube actuator.

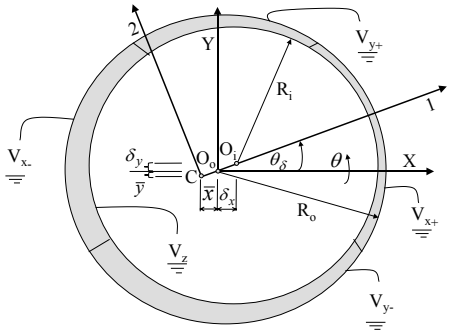

Fig. 2. Cross-section of the piezoelectric tube actuator.

The outer and inner radii are R_o and R_i, respectively. The angle θ is measured from the X-axis.

The model is based on elementary bending theory for thin-walled members. The main assumptions are small deformations and angles, that plane sections of the tube remain plane after deformation, material is linear elastic, and negligible effects of rotatory inertia and shear deformation. The rotatory inertia of the end mass m_o and tube are also neglected. The first step in deriving the model is finding the centroid C of the cross section. The coordinates of the centroid $\bar{x}$ and $\bar{y}$ relative to O_o are giving by

$$\bar{x} = \frac{\int x dA}{\int dA} = \frac{\int_0^{2\pi}\int_{R_{i(\theta)}}^{R_o} r^2 cos(\theta) dr d\theta}{\pi(R_o^2 - R_i^2)} \quad (1)$$

$$\bar{y} = \frac{\int y dA}{\int dA} = \frac{\int_0^{2\pi}\int_{R_{i(\theta)}}^{R_o} r^2 sin(\theta) dr d\theta}{\pi(R_o^2 - R_i^2)} \quad (2)$$

where

$$R_\delta = \sqrt{\delta_x^2 + \delta_y^2}\ , \quad \theta_\delta = tan^{-1}(\frac{\delta_y}{\delta_x}) \quad (3)$$

$$R_i(\theta) = R_\delta cos(\theta - \theta_\delta) + \sqrt{R_i^2 - R_\delta^2\, sin^2(\theta - \theta_\delta)}$$

For a positive δ_x and δ_y, the centroid will be located below and to the left of O_o. Because of the eccentricity, the X and Y axes are no longer the principal axes of inertia, i.e. axes along which lateral deflection occurs. The new principal axes of inertia 1 and 2 can be found from symmetry. Axis 1 is along the point of minimum thickness at θ_δ, while the 2-axis is perpendicular to it. The Z-axis (or 3-axis) passes through the centroid C. For thin-walled members, the only stress is assumed to be in the Z-direction. Therefore, the linear constitutive relation for piezoelectric material [7] reduces to

$$\begin{pmatrix} \epsilon_z \\ D_r \end{pmatrix} = \begin{pmatrix} s_{11}^E & d_{31} \\ d_{31} & \epsilon_3^\sigma \end{pmatrix} \begin{pmatrix} \sigma_z \\ E_r \end{pmatrix} \quad (4)$$

where σ_z is the stress, ϵ_z is the strain, D_r is the electric displacement, E_r is the applied electric field, and subscript r denotes the radial direction. The electric field E_r will be assumed constant over the tube thickness.

Assuming constant inertia $\rho_p A_p$ per unit length, where ρ_p is the density and A_p is the cross sectional area, the equation of motion in the 1-direction is

$$\rho_p A_p \frac{\partial^2 u_{1p}}{\partial t^2} + b_{p1}\frac{\partial u_{1p}}{\partial t} = \frac{\partial F_{1sp}}{\partial z} \quad (5)$$

where b_{p1} is the viscous damping coefficient, and F_{1sp} is the shear force in the 1-direction. The shear force is related to the bending moment by $F_{1sp} = -\partial M_{2p}/\partial z$, where the bending moment is given by

$$M_{2p} = -\int\int r cos(\theta + \theta_\delta)\, \sigma_z\, d\theta\, dr \quad (6)$$

In Equation (6), the limits of integration with respect to r are from R_{C_i} to R_{C_o}; the distances from C to the inner and outer cylinders, respectively. The variation of the radii with respect to θ, is given by

$$R_{C_i} = R_{CO_i} cos(\theta - \theta_\delta) + \sqrt{R_i^2 - R_{CO_i}^2 sin^2(\theta - \theta_\delta)} \quad (7)$$

$$R_{C_o} = R_{CO_o} cos(\theta - \theta_\delta) + \sqrt{R_o^2 - R_{CO_o}^2 sin^2(\theta - \theta_\delta)} \quad (8)$$

and

$$R_{CO_i} = \sqrt{(\bar{x} - \delta_x)^2 + (\bar{y} - \delta_y)^2} \quad (9)$$

$$R_{CO_o} = \sqrt{(\bar{x}^2 + \bar{y}^2)} \quad (10)$$

where R_{CO_i} and R_{CO_o} are the distances from C to O_i and O_o, respectively, and R_i and R_o are the radii of the inner and outer cylinders measured from their own geometric center as seen in Figure 2. Substituting the first equation of (4) into (6) and integrating with respect to r, leads to

$$M_{2p} = \int_0^{2\pi} [\frac{(R_{Co}^4 - R_{Ci}^4)\, cos^2(\theta + \theta_\delta)}{4\, R_{curv_{1p}}\, s_{11}^E} - \frac{d_{31}(R_{Co}^3 - R_{Ci}^3) cos(\theta + \theta_\delta) E_r}{3 s_{11}^E}]\, d\theta$$

$$= \frac{\alpha_{u_{1p}}}{s_{11}^E\, R_{curv_{1p}}} + M_{2_V}(V) \quad (11)$$

$$M_{2_V} = -\int_0^{2\pi} \frac{d_{31}(R_{Co}^3 - R_{Ci}^3) cos(\theta + \theta_\delta) V}{3 s_{11}^E (R_{Co} - R_{Ci})} d\theta \quad (12)$$

$$M_{2_V} = -\frac{d_{31}}{s_{11}^E}\sum_j \gamma_j V_j \quad (13)$$

where

$$
\begin{aligned}
V &= \begin{cases} V_{x_+} - V_z & -\frac{\pi}{4} < \theta < \frac{\pi}{4} \\ V_{y_+} - V_z & \frac{\pi}{4} < \theta < \frac{3\pi}{4} \\ V_{x_-} - V_z & \frac{3\pi}{4} < \theta < \frac{5\pi}{4} \\ V_{y_-} - V_z & \frac{5\pi}{4} < \theta < \frac{7\pi}{4} \end{cases} \qquad (14) \\
j &= [x_+, x_-, y_+, y_-, z] \\
\gamma_{x_+} &= \int_{-\pi/4}^{\pi/4} \frac{(R_{Co}^3 - R_{Ci}^3) cos(\theta + \theta_\delta)}{3(R_{Co} - R_{Ci})} \, d\theta
\end{aligned}
$$

where M_{2p} is the bending moment about the 2-axis, M_{2_V} is the bending moment about the 2-axis due to the applied voltages, and $R_{curv_{1p}}$ is the radius of curvature of the deformed tube in the $1-Z$ plane, which is related to u_{1p}, for small deformations by

$$\frac{1}{R_{curv_{1p}}} = \frac{\partial^2 u_{1p}}{\partial z^2} \qquad (15)$$

Substituting Equations (11) and (15) into Equation (5), results in

$$\rho_p A_p \frac{\partial^2 u_{1p}}{\partial t^2} + b_{p1} \frac{\partial u_{1p}}{\partial t} + \frac{\alpha_{u_{1p}}}{s_{11}^E} \frac{\partial^4 u_{1p}}{\partial z^4} = 0 \qquad (16)$$

The boundary conditions are zero deflection and slope at the fixed end $z = 0$, and a balance of forces in the 1-direction and zero moment about the 2-axis at the free end. Mathematically, the conditions are

At $z = 0$

$$
\begin{aligned}
u_{1p} &= 0 \qquad (17) \\
\frac{\partial u_{1p}(0,t)}{\partial z} &= 0 \qquad (18)
\end{aligned}
$$

At $z = L_p$

$$
\begin{aligned}
F_{1r}(t) &= m_o \frac{\partial^2 u_{1p}(L_p,t)}{\partial t^2} + b_{p1} \int_0^{L_p} \frac{\partial u_{1p}(z,t)}{\partial t} dz \\
&\quad + \frac{\alpha_{u_{1p}}}{s_{11}^E} \frac{\partial^3 u_{1p}}{\partial z^3} \qquad (19) \\
-M_{2_V} &= \frac{\alpha_{u_{1p}}}{s_{11}^E} \frac{\partial^2 u_{1p}}{\partial z^2} \qquad (20)
\end{aligned}
$$

The concentrated loads $F_{1r}(t)$ and M_{2_V} appearing in Equations (19) and (20) result in time-dependant boundary conditions. As a result, the technique of separation of variables could not be used to solve for the deflection. Some authors have suggested moving the time-dependant terms from the boundary conditions and including them in the equation of motion as concentrated loads. However, using this method would result in mode shapes that would not converge in satisfying the "true boundary conditions" regardless of the number of terms retained in the summation of modes. Alternatively, it is possible to use techniques as outlined in [8]. However, the resulting transfer function model of the system would be proper (number of zero equals the number of the poles). Consequently, that model would not capture the high-frequency magnitude roll-off observed in an experimental frequency response. Alternatively, an approximate solution can be used to arrive at a low-order model that captures the number of modes of interest. An n^{th} mode model based on Rayleigh-Ritz method will be formulated. The deflection u_{1p} is approximated by a finite sum as

$$u_{1p}(z,t) \approx \sum_{i=1}^{n} \psi_{1pi}(z) \, T_{1pi}(t) \qquad (21)$$

where ψ_{1pi} are trial functions that satisfy the geometric (displacement and rotation) boundary conditions but not necessarily the natural (force and moment) boundary conditions. The resulting model is

$$M \ddot{T}_{1p} + C \dot{T}_{1p} + K T_{1p} = Q_{1p} \begin{bmatrix} F_{1r}(t) \\ \frac{d_{31}}{s_{11}^E} \sum_j \gamma_j V_j \end{bmatrix} \qquad (22)$$

where $T_{1p} = [T_{1p1} ... T_{1pi}]^T$, M is the mass matrix, K is the stiffness matrix, C is the damping coefficient matrix, and Q_{1p} is the generalized loads input matrix. The elements of these matrices are given by

$$
\begin{aligned}
m_{ij} &= \rho_p A_p \int_0^{L_p} \psi_{1pi}(z) \psi_{1pj}(z) dz \qquad (23) \\
&\quad + m_o \psi_{1pi}(L_p) \psi_{1pj}(L_p) \qquad (24) \\
c_{ij} &= b_{p1} \int_0^{L_p} \psi_{1pi}(z) \psi_{1pj}(z) dz \qquad (25) \\
k_{ij} &= \frac{\alpha_{u_{1p}}}{s_{11}^E} \int_0^{L_p} \frac{\partial^2 \psi_{1pi}(z)}{\partial z^2} \frac{\partial^2 \psi_{1pj}(z)}{\partial z^2} dz \qquad (26) \\
q_{1pi} &= [\psi_{1pi}(L_p) \quad \frac{\partial \psi_{1pi}(L_p)}{\partial z}] \qquad (27)
\end{aligned}
$$

For a two-mode model with $\psi_{1p1}(z) = z^2$ and $\psi_{1p2}(z) = z^3$, the resulting model is given by

$$
\begin{aligned}
M &= \begin{bmatrix} \rho_p A_p \frac{L_p^5}{5} + m_o L_p^4 & \rho_p A_p \frac{L_p^6}{6} + m_o L_p^5 \\ \rho_p A_p \frac{L_p^6}{6} + m_o L_p^5 & \rho_p A_p \frac{L_p^7}{7} + m_o L_p^6 \end{bmatrix} \qquad (28) \\
Q_{1p} &= \begin{bmatrix} L_p^2 & 2L_p \\ L_p^3 & 3L_p^2 \end{bmatrix}, \; C = b_{p1} \begin{bmatrix} \frac{L_p^5}{5} & \frac{L_p^6}{6} \\ \frac{L_p^6}{6} & \frac{L_p^7}{7} \end{bmatrix} \qquad (29) \\
K &= \frac{\alpha_{u_{1p}}}{s_{11}^E} \begin{bmatrix} 4L_p & 6L_p^2 \\ 6L_p^2 & 12L_p^3 \end{bmatrix} \qquad (30)
\end{aligned}
$$

It is worth noting that as a result of machining, actual tubes are not perfectly round. In addition, the wall thickness may vary along the tube's length. This can be handled in the model by using the desired thickness distribution as a function of θ, and depth z, in Equation (6). However, this will only change the coefficients γ_i, and α_i slightly, but the structure of the model will remain unchanged. Finally, the equation of motion for u_{2p} can be derived similarly.

B. Piezoelectric Tube Longitudinal Dynamics

Under similar assumptions of those in Section II-A, the equation of motion for the tube's extension u_{3p} is given by

$$\rho_p A_p \frac{\partial^2 u_{3p}}{\partial t^2} + b_{p3} \frac{\partial u_{3p}}{\partial t} = \frac{\partial F_{3p}}{\partial z} \qquad (31)$$

where

$$F_{3p} = \int \sigma_z dA_p = \frac{1}{s_{11}^E}\int [\epsilon_z - d_{31}E_r]dA_p = \frac{1}{s_{11}^E}\int \epsilon_z dA_p - \frac{d_{31}}{s_{11}^E}\sum_j \gamma_{3j}V_j \quad (32)$$

and

$$j = [x_+, x_-, y_+, y_-, z]$$
$$\gamma_{3j} = \int [R_o + R_i(\theta)]\, V_j(\theta)\, d\theta \quad (33)$$

Substituting Equation (32) into (31), results in

$$\rho_p A_p \frac{\partial^2 u_{3p}}{\partial t^2} + b_{p3}\frac{\partial u_{3p}}{\partial t} - \frac{A_p}{s_{11}^E}\frac{\partial^2 u_{3p}}{\partial z^2} = 0 \quad (34)$$

where b_{p3} is the coefficient of viscous damping. The boundary conditions are zero displacement at the fixed end $z = 0$, and a balance of forces at the other end $z = L_p$, which can be expressed as

At $z = 0$

$$u_{3p} = 0 \quad (35)$$

At $z = L_p$

$$m_o\frac{\partial^2 u_{3p}(L_p,t)}{\partial t^2} + b_{p3}int_0^{L_p}\frac{\partial u_{3p}(z,t)}{\partial t}dz + \frac{A_p}{s_{11}^E}\frac{\partial^2 u_{3p}}{\partial z^2} = +\frac{d_{31}}{s_{11}^E}\sum_j \gamma_{3j}V_j + \frac{s_{11}^E}{A_p}F_{3r}(t) \quad (36)$$

The solution to Equation (34) can be obtained by means of a finite sine Fourier transform which is given by

$$U_{3p}(n,t) = \int_0^{L_p} u_{3p}(z,t)sin(nz)\, dz \quad (37)$$

Taking the Fourier transform of Equation (34) results in

$$\rho_p A_p \frac{\partial^2 U_{3p}}{\partial t^2} + b_{p3}\frac{\partial U_{3p}}{\partial t} - \frac{A_p}{s_{11}^E}\frac{\partial^2 U_{3p}}{\partial z^2} = 0 \quad (38)$$

where it is assumed that

$$\int_0^{L_p}\frac{\partial^2 u_{3p}}{\partial t^2}sin(nz)dz = \frac{\partial^2}{\partial t^2}\int_0^{L_p} u_{3p}(z,t)sin(nz)dz = \frac{\partial^2 U_{3p}(n,t)}{\partial t^2} \quad (39)$$

The Fourier transform of $\frac{\partial^2 u_{3p}}{\partial z^2}$ is given by

$$\frac{\partial^2 U_{3p}(n,t)}{\partial z^2} = \int_0^{L_p}\frac{\partial^2 u_{3p}(z,t)}{\partial z^2}sin(nz)dz = [\frac{\partial u_{3p}(z,t)}{\partial z}sin(nz) - nu_{3p}(z,t)cos(nz)]_0^{L_p} - n^2 U_{3p}(n,t) \quad (40)$$

By using the boundary conditions of Equations (35) and (36), Equation (40) reduces to

$$\frac{\partial^2 U_{3p}(n,t)}{\partial z^2} = sin(nL_p)[F_a(t) - \frac{s_{11}^E m_o}{A_p}\frac{\partial^2 u_{3p}(L_p,t)}{\partial t^2} - \frac{s_{11}^E b_{p3}}{A_p}\int_0^{L_p}\frac{\partial u_{3p}(z,t)}{\partial t}dz] - nu_{3p}(L_p,t)cos(nL_p) - n^2 U_{3p}(n,t) \quad (41)$$

$$F_a(t) = \frac{d_{31}}{s_{11}^E}\sum_j \gamma_{3j}V_j + \frac{s_{11}^E}{A_p}F_{3r}(t) \quad (42)$$

Since $\frac{\partial^2 u_{3p}(L_p,t)}{\partial t^2}$, $\frac{\partial u_{3p}(L_p,t)}{\partial t}$, and $u_{3p}(L_p,t)$ are not known, they can be eliminated from Equation (41) by setting the sum of their terms to zero which gives

$$n_i L_p tan(n_i L_p) = \frac{\rho_p A_p L_p}{m_o} \quad (43)$$

which can be solved for p_n. The natural frequencies ω_{3pn} are given by $\omega_{3pn} = \frac{n_i}{\sqrt{\rho_p s_{11}^E}}$. As a result, Equation (41) reduces to

$$\frac{\partial^2 U_{3p}(n_i,t)}{\partial z^2} = F_a(t)sin(n_i L_p) - n_i^2 U_{3p}(n_i,t) \quad (44)$$

Hence, Equation (38) becomes

$$\rho_p A_p \frac{d^2 U_{3p}(n_i,t)}{dt^2} + b_{p3}\frac{dU_{3p}(n_i,t)}{dt} + \frac{A_p}{s_{11}^E}n_i^2 U_{3p}(n_i,t) = \frac{A_p}{s_{11}^E}sin(n_i L_p)F_a(t) \quad (45)$$

with initial conditions

$$U_{3p}(n_i,0) = \int_0^{L_p} u_{3p}(z,0)sin(n_i z)dz$$
$$U_{3p}(n_i,0) = \int_0^{L_p}\frac{\partial u_{3p}(z,0)}{\partial t}sin(n_i z)dz \quad (46)$$

The displacement $u_{3p}(z,t)$ can be found by inverse Fourier transform given by

$$u_{3p}(z,t) = \frac{2}{L_p}\sum_{n=1}^{\infty} U_{3p}(n_i,t)\, sin(n_i z) \quad (47)$$

C. Hysteresis and Nonlinear Displacement Sensitivity

Piezoelectric materials are ferroelectric, hence, they exhibit hysteretic relationship between some of the electric variables (electric field and electric displacement) and the mechanical variables (mechanical strain and force). Hysteresis in piezoelectric materials [9]–[11], is generally attributed to molecular friction at sites of material imperfections as a result of domain walls motion. In the absence of an applied electric field, domain walls form at pinning sites to minimize associated potential energy. When a small electric field is applied, domain walls motion is limited and reversible, hence hysteresis in not observed. At higher magnitudes of electric field, the local energy barriers associated with the pinning

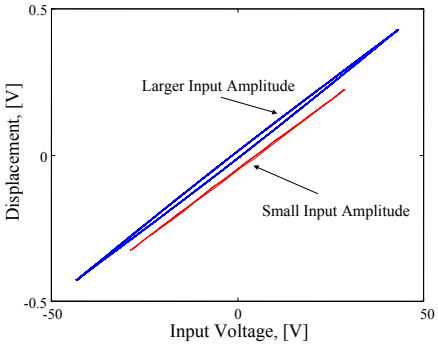

Fig. 3. Experiments using a sinusoidal input voltage at 300 Hz with two different amplitudes.

sites are overcome and domain walls move an extended distance. The motion of domain walls across pinning sites provide an irreversible mechanism that contributes to the observed hysteresis. The experimental observations of absence and existence of hysteresis at low and high electric fields, respectively, is demonstrated in Fig. 3. The figure shows experimental voltage to mechanical displacement response of a PZT-5H piezoelectric tube actuator for a sinusoidal input at 300Hz and two voltage amplitudes. It is worth mentioning that the first mechanical resonance of this particular actuator is at $9.7\,kHz$. Hence, the experiment is considered quasisteady.

In practice, the electric field applied to a piezoelectric actuator is limited to avoid saturation and degradation in the actuator performance. Therefore, typical hysteresis loops can be characterized by their average slope, loop center point, and loop width. These characteristics strongly depend on the piezoelectric compound. In a quasisteady hysteresis experiment, the frequency of the periodic input voltage signal should be much lower than the first mechanical resonance. In addition, it should be chosen to be fast enough such that creep response is not observed. Under these conditions, the width of the measured hysteresis loop will be independent of the input frequency, i.e. rate-independent. The rate independence nature of piezoelectric hysteresis has been experimentally verified by several authors [12]–[14].

Hysteresis has been extensively studied in the literature. As a result, there are various models of varying complexity that may be used to model hysteresis. Examples include Preisach [15], [16], Krasnosel'skii and Pokrovskii [17], the Generalized Maxwell Slip model [18], Bouc-Wen [19], [20], Dahl [21], Chua-Stromsmoe [22], [23], and Coleman-Hodgdon [24].

In piezoelectric materials energy transduction occurs between electrical and mechanical domains. As discussed earlier, impediment of domain wall motion contributes to hysteresis. However, it is not clear whether there are other mechanisms in the mechanical domain that contribute to the observed hysteresis. Answering this question allows including a physically consistent hysteresis model in the overall model of a piezoelectric actuator. As before, it has been suggested

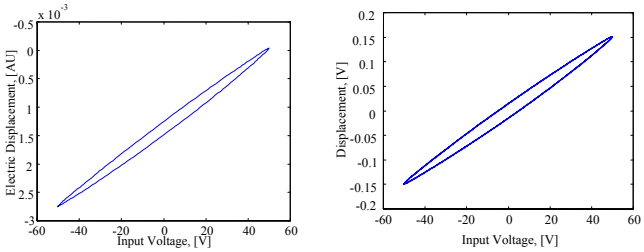

Fig. 4. Piezoelectric actuator response to a sinusoidal input voltage at $20\,Hz$ (a) electrical displacement (arbitrary units AU) vs. input voltage, (b) mechanical displacement vs. input voltage.

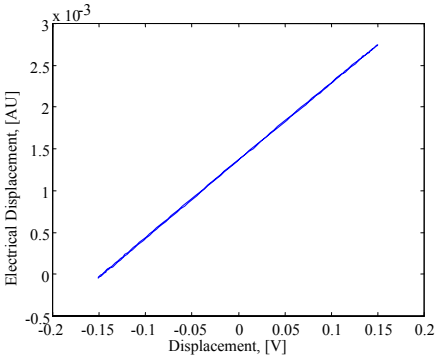

Fig. 5. Piezoelectric actuator response to a sinusoidal input voltage at $20\,Hz$: electrical displacement (arbitrary units AU) vs. mechanical displacement.

that hysteresis occurs in the electrical domain between the applied electric field and electric displacement or charge. This is supported by experimental observations as in Fig. 4 (a). Hysteresis is also observed, Fig. 4 (b), between electric field and mechanical strain or displacement. In addition, hysteresis is noticed between force and mechanical strain [14], when actuator electrodes are shorted and charge is allowed to flow. However, no hysteresis is observed when electrodes are open and no charge flows within the material. More so, charge vs. mechanical strain as in Fig. 5, shows no hysteresis. Accordingly, hysteresis is believed to lie mainly in the electrical domain.

To include hysteresis in the piezoelectric tube model, its effect will be lumped into a single hysteretic element. Due to hysteresis, the applied electric field E_r, is balanced by a potential drop E_h, due to the combined capacitance and resistance of the hysteretic element, in addition to a drop E_p, across the hysteresis-free capacitance of the piezoelectric material as

$$E_r = E_h + E_p \tag{48}$$

The models of sections II-A and II-B, were derived assuming that $E_r = E_p$ in the piezoelectric constitutive relation Equation (4). The new constitutive relation is obtained by replacing E_r with E_p which gives

$$\begin{pmatrix} \epsilon_z \\ D_r \end{pmatrix} = \begin{pmatrix} s_{11}^E & d_{31} \\ d_{31} & \epsilon_3^\sigma \end{pmatrix} \begin{pmatrix} \sigma_z \\ E_p \end{pmatrix} \tag{49}$$

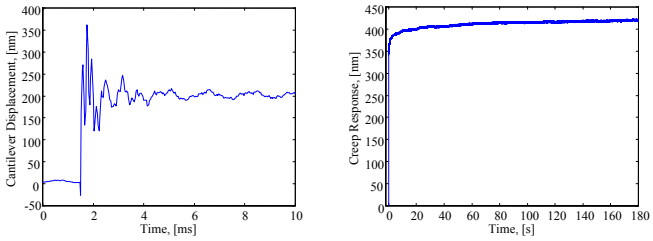

(a) (b)

Fig. 6. Two creep experiments: (a) initial fast response, (b) slow creep response.

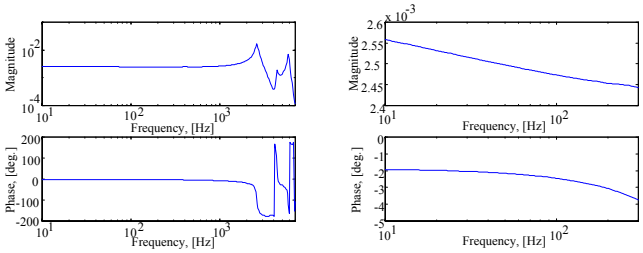

(a) (b)

Fig. 7. Experimental frequency response between input voltage and displacement of a PZT-5H actuator (a) Full frequency range, (b) zoom on 10 to 300 Hz range.

In addition, the electric charge in the actuator q_p, is given by

$$q_p = \int D_r \, dA_p \tag{50}$$

As a result, Equations (22) and (42), know become

$$M \ddot{T}_{1p} + C \dot{T}_{1p} + K T_{1p} = Q_{1p} \begin{bmatrix} F_{1r}(t) \\ \frac{d_{31}}{s_{11}^E} \sum_j \gamma_j (V_j - k_{1jh} V_h) \end{bmatrix}$$

$$F_a(t) = \frac{d_{31}}{s_{11}^E} \sum_j \gamma_{3j} (V_j - k_{3jh} V_h) + \frac{s_{11}^E}{A_p} F_{3r}(t) \tag{51}$$

where k_{1jh} and k_{3jh} are constants introduced to account for the fact that not the whole piezoelectric material necessarily contributes to hysteretic behavior. A hysteresis model in addition to Equations (48) and (50) are used to express the relationship between electric charge and the potential across the hysteresis element V_h. The anhysteretic voltage to displacement curve may be used to model the nonlinear voltage to displacement sensitivity of the piezoelectric actuator.

D. Creep

The displacement response of a piezoelectric actuator to a rapid change in input voltage as shown in Fig. 6, consists of two main parts. The initial part of the response occurs over a time scale dictated by the mechanical resonance of the actuator, typically few millisecond. This is followed by a slow creeping response occurring over tens to hundreds of seconds and could amount to more than $20\,\%$ of the total response. The rate and amount of creep, strongly depend on the piezoelectric compound. As discussed in Section II-C, pinning sites impede on the motion of domain walls. When an electric field is applied to the material, the domain walls will eventually align in a way to conform with the applied electric field. The initial fast response would be due to domain walls experiencing little resistance and their response would be limited by the maximum mechanical strain rate of the material. Other domain walls, on the other hand, would experience much more resistance to their motion. The effective capacitance and path resistance of these domain walls, will dictate the amount of motion and time scale over which this motion occurs. This could amount to the creep response.

The aforementioned discussion on the origin of creep, may suggest that a model composed of capacitive and resistive

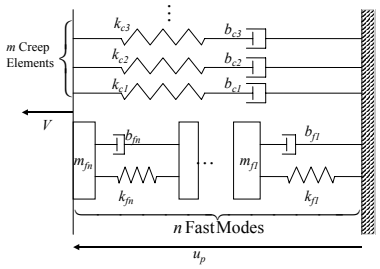

Fig. 8. Schematic representation of a model for both fast and creep dynamics.

elements may be appropriate. Furthermore, experimental frequency response of piezoelectric actuators shown in Fig. 7 (a), displays very little variation in phase at low frequency between input voltage and displacement, Fig. 7 (b). Moreover, as seen in Fig. 7 (b), a slight decrease in gain is observed with increased frequency; 4.5% from $10\,Hz$ to $300\,Hz$. Therefore, a transfer function model between the input voltage and actuator displacement would have a relative degree zero at frequencies much lower than the actuator's first resonance frequency. The relative degree is defined as the number of poles minus the number of zeros of the transfer function. It is possible therefore, to simulate creep behavior using a suitable LTI model composed of capacitive and resistive elements. A schematic representation of the overall dynamic model including a creep model is shown in Fig. 8. Its mathematical representation for the actuator vertical dynamics with V_z as input is given as

$$\begin{aligned} \frac{u_p}{V} &= \frac{b_{m+n-2} s^{m+n-2} + b_{m+n-3} s^{m+n-3} + \ldots + b_0}{s^{m+n} + a_{m+n-1} s^{m+n-1} + \ldots + a_0} \\ &= G_f(s)\, G_{creep}(s) \end{aligned} \tag{52}$$

where G_f is the transfer function containing the fast dynamics and retains n poles and $n-2$ zeros as suggested by the models presented in Sections II-A and II-B. G_{creep} is the transfer function modeling the creep which has a zero relative degree and contains m poles. The model assumes that the ratio between the amount of creep and the fast actuator displacement is independent of input amplitude and rate. Both assumption have been experimentally verified [25].

III. Discussion

The physically based model presented within can be tailored to be of low or high-order linear or nonlinear depending on what the model will be used for. In contrast to experimentally identified models such as [4], it is not specific to a particular actuator and can be generally used for quasistatic or dynamic analysis and design for either open or closed loop systems. The equations governing the displacements of the tube's free end and rotations about X and Y axes, namely θ_{px} and θ_{py} are given by

$$x_p(t) = cos(\theta_\delta)\, u_1(L_p,t) - sin(\theta_\delta)\, u_2(L_p,t) \quad (53)$$

$$y_p(t) = sin(\theta_\delta)\, u_1(L_p,t) + cos(\theta_\delta)\, u_2(L_p,t) \quad (54)$$

$$z_p(t) = u_{3p}(L_p,t) \quad (55)$$

$$\theta_{px}(t) = sin(\theta_\delta)\, \frac{\partial u_1}{\partial z} + cos(\theta_\delta) \frac{\partial u_2}{\partial z} \quad (56)$$

$$\theta_{py}(t) = cos(\theta_\delta)\, \frac{\partial u_1}{\partial z} - sin(\theta_\delta) \frac{\partial u_2}{\partial z} \quad (57)$$

In an ideal concentric and symmetric tube actuator, applying a voltage signal V_z to command a displacement in the Z-direction, results in no lateral displacement. Practically, however, a coupled response is observed. This can be seen from Equations (22) and (42) for which a nonzero γ_z results from eccentricity in the actuator. Similarly, lateral displacement causes a vertical displacement due to the applied voltage in addition to a geometric coupling. Geometric coupling is inherent in the construction of this tube actuator since lateral displacements result from actuator bending which causes the actuator's length (in Z-axes) to shrink slightly. As an illustration for coupling, consider the case where creep and hysteresis effects are ignored. The transfer function between the lateral displacement x_p and the voltage for vertical displacement V_z is given as

$$x_p(s) = \sum_{j=1}^{\infty} \frac{k_{jz}\, V_z}{s^2 + 2\zeta_{\theta_j}\omega_{\theta_j} s + \omega_{\theta_j}^2} \quad (58)$$

where, ζ is damping ratio, ω is natural frequency, and k_{jz} is a constant. Accordingly, in applications where the actuator is used to provide both lateral and vertical displacements, the voltage corresponding to vertical displacement V_z will produce lateral displacements governed by Equation (58). These displacements will be seen as disturbances to the main lateral response corresponding to V_x and V_y. The resonance frequency for the lateral dynamics is inherently lower than that of the longitudinal dynamics. Therefore, V_z is expected to contain frequencies that may excite the lateral resonances acting as an out of bandwidth disturbance. Accordingly, this disturbance will not be well compensated for either in open or closed loop control.

As a demonstration for effects of coupling, a setup consisting of a tube actuator with an optical sensor measuring the angle θ_{py} of the actuator's free end was used. The tube is of type PZT-5A with length $44.4\,mm$, outer diameter $6.35\,mm$, and wall thickness $0.5\,mm$. The density is $7500\ kg/m^3$, $d_{31} = -1.73 \times 10^{-10}\, m/V$, $s_{11}^E = 15.9 \times 10^{-12}\, m^2/N$, and maximum input voltage of $\pm 200V$. The eccentricity

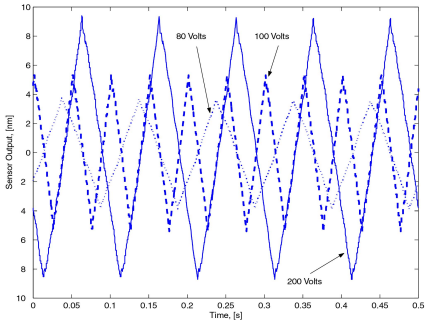

Fig. 9. Sensor output due to coupling between actuator longitudinal and lateral motions for different values of V_z.

is assumed to be $\delta_x = 49.5\,\mu m$ and $\delta_y = 5\,\mu m$. The resulting model has sensitivity of $1.38^{-7}\, rad/V$ between θ_{py} and V_z. Quasisteady effect of coupling was measured by applying a low-frequency ($10\,Hz$) triangular wave as V_z and measuring θ_{py} with the optical sensor. The results are shown in Fig. 9, for 3 different voltage amplitudes, namely ± 80, ± 100 and $\pm 200\,V$. The resulting sensor output corresponds approximately to 7.6, 10.7, and $18.1\,nm$ peak-to-peak. Based on the sensitivity of the model and the cantilever's nominal length, the changes in sensor output predicted by the model are 5.5, 6.9, and $13.8\,nm$ for ± 80, ± 100 and $\pm 200\,V$. The model gives a good agreement with experiments, considering the fact the actual eccentricity of the tube was not measured for use in the model.

The dynamic effects of coupling can be seen in Fig. 10 which shows an experimental time response of the actuator's angle due to a $40\,V$ step in V_z. The response is initially dominated by the fast modes that are observable at the output which are in the kHz range. The response eventually becomes dominated by the actuator first bending dynamics at $400\,Hz$ as the faster dynamics die out. As discussed previously, this response to the vertical voltage command V_z is an out of bandwidth disturbance to the main lateral response. Accordingly, bending modes become observable for certain output measurements. Therefore, to avoid exciting the first bending mode, a large reduction in the bandwidth of vertical motion would be required to preserve performance in open loop actuator control and stability and performance in closed loop control.

IV. Summary and Conclusion

The paper presented a new model for a piezoelectric tube actuator commonly used in many high-precision instruments. The model captures the coupling between motion in all three axes such as bending motion due to a supposedly pure extension of the actuator. A discussion on the origin of hysteresis is presented and experimental data is provided as a physical reasoning of how a hysteresis model is included in the overall dynamic model. This also allows modeling nonlinear sensitivity in the voltage to displacement response. Moreover, a model for creep phenomenon is included to capture the observed slow response due to a sudden change in input voltage. Experiential

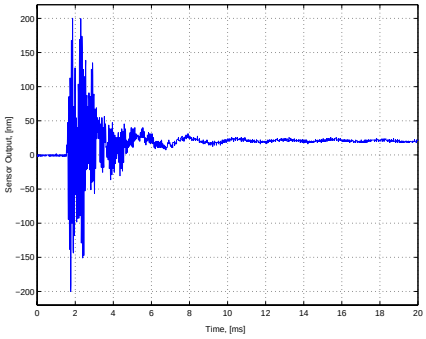

Fig. 10. Sensor output for a 40 V step in V_z.

data on creep is also used to support the model. Results show that due to coupling a voltage corresponding to vertical displacement V_z will produce lateral displacement that acts as a disturbance to the main lateral response. The resonance frequency for the lateral dynamics is inherently lower than that of the longitudinal dynamics. Therefore, V_z is expected to contain frequencies that may excite the lateral resonances. Accordingly, this out of bandwidth disturbance will not be well compensated for either in open or closed loop control of the actuator. Consequently, to avoid exciting the first bending mode, a large reduction in the bandwidth of vertical motion would be required. The models presented within can be used for linear and nonlinear analysis and controller design for the actuator.

ACKNOWLEDGMENT

The authors would like to thank the Singapore-MIT Alliance and King Abdulaziz City for Science and Technology, Riyadh, Saudi Arabia for their support of this work.

REFERENCES

[1] M. E. Taylor, "Dynamics of piezoelectric tube scanners for scanning probe microscopy," *Review of Scientific Instruments*, vol. 64, no. 1, pp. 154–158, January 1993.

[2] S. Yang and W. Huang, "Transient response of a piezoelectric tube scanner," *Review of Scientific Instruments*, vol. 68, no. 12, pp. 4483–4487, 1997.

[3] T. Ohara and K. Youcef-Toumi, "Dynamics and control of piezotube actuators for subnanometer precision applications," in *Proc. American Control Conference*, Seattle, Washington, USA, June 1995, pp. 3808–3812.

[4] G. Schitter and A. Stemmer, "Fast closed loop control of piezoelectric transducers," *Journal of Vacuum Science and Technology B*, vol. 20, no. 1, pp. 350–352, Jan./Feb. 2002.

[5] N. Tamer and M. Dahleh, "Feedback control of piezoelectric tube scanners," in *Proce. of the 33rd IEEE Conference on Decision and Control*, vol. 2, Dec. 5–9, 1994, pp. 1826 –1831.

[6] *EBL Product Line Catalog*, Stavely Sensors Inc., 91 Prestige Park Circle, East Hartford, CT 06108-1918.

[7] *IEEE Standard on Piezoelectricity*, ANSI/IEEE Std 176-1987, 1987.

[8] R. Mindlin and L. Goodman, "Beam vibrations with time-dependant boundary conditions," *Journal of Applied Mechanics*, vol. 17, pp. 377–380, 1950.

[9] R. Smith and Z. Ounaies, "A domain wall model for hysteresis in piezoelectric materials," Institute for Computer Applications in Science and Engineering, NASA Langley Research Center, Tech. Rep. NASA/CR-1999-209832 and ICASE Report No. 99-52, 1999.

[10] I.-W. Chen and Y. Wang, "A domain wall model for relaxor ferroelectrics," *Ferroelectrics*, vol. 206, pp. 245–263, 1998.

[11] V. Fedosov and A. Sidorkin, "Quasielastic displacements of domain boundaries in ferroelectrics," *Soviet Physics Solid State*, vol. 18, no. 6, pp. 964–968, 1976.

[12] W. d. K. H.J. Adriaens and R. Banning, "Modeling piezoelectric actuators," *IEEE/ASME Transaction on Mechatronics*, vol. 5, no. 4, pp. 331–341, December 2000.

[13] D. Hughes and J. Wen, "Preisach modeling of piezoceramic and shape memory alloy hysteresis," in *Smart Materials and Structures*, vol. 6, 1997, pp. 287–300.

[14] M. Goldfarb and N. Celanovic, "Modeling piezoelectric stack actuators for control of micromanipulation," *IEEE Control Systems Magazine*, vol. 17, no. 3, pp. 69–79, June 1997.

[15] F. Preisach, "Uber die magnetische nachwirkung," *Zeitschrift fur Physik*, vol. 94, pp. 277–302, 1935.

[16] I. D. Mayergoyz91, *Mathematical Models of Hysteresis*. New York: Springer-Verlag, 1991.

[17] M. Krasnosel'skii and A. Pokrovskii, *Systems with Hysteresis*. Berlin: Springer-Verlag, 1989.

[18] B. Lazan, *Damping of Materials and Members in Structural Mechanics*. London: Pergamon Press, 1968.

[19] R. Bouc, "Forced vibration of mechanical system with hysteresis," in *Proceedings of* 4^{th} *Conference on Nonlinear Oscillations*, Parague, Czechoslovakia, 1967, p. 315.

[20] Y.-K. Wen, "Methods for random vibration of hysteretic systems," *Journal of the Engineering Mechanics Division EM2*, pp. 249–263, April 1976.

[21] P. Dahl, "Solid friction damping of mechanical vibrations," *American Institute of Aeronautics and Astronautics Journal*, vol. 14, no. 12, pp. 1675–1682, Dec. 1976.

[22] L. Chua and K. Stromsmoe, "Mathematical model for dynamic hysteresis loops," *International Journal of Engineering Science*, vol. 9, pp. 435–450, 1971.

[23] L. Chua and S. Bass, "A generalized hysteresis model," *IEEE Transactions on Circuit Theory*, vol. CT-19, no. 1, pp. 36–48, Jan. 1972.

[24] B. Coleman and M. Hodgdon, "A constitutive relation for rate-independent hysteresis in ferromagnetically soft materials," *International Journal of Engineering Science*, vol. 24, no. 6, pp. 897–919, 1986.

[25] O. M. El Rifai, "Modeling and control of undesirable dynamics in atomic force microscopes," Ph.D. dissertation, MIT, Cambridge, MA, USA, 2002.